Nanoscale

ROYAL SOCIETY OF CHEMISTRY

PAPER

View Article Online
View Journal | View Issue



Cite this: *Nanoscale*, 2022, **14**, 3200

# On the mechanical properties and fracture patterns of the nonbenzenoid carbon allotrope (biphenylene network): a reactive molecular dynamics study†

M. L. Pereira, Júnior, [b] W. F. da Cunha,[a] R. T. de Sousa, Junior, [b] G. D. Amvame Nze,[b] D. S. Galvão[c,d] and L. A. Ribeiro, Júnior *[a]

Recently, a new two-dimensional carbon allotrope named biphenylene network (BPN) was experimentally realized. The BPN structure consists of four-, six-, and eight-membered rings of $sp^2$-hybridized carbon atoms. In this work, we carried out fully-atomistic reactive (ReaxFF) molecular dynamics simulations to study the mechanical properties and fracture patterns of non-defective and defective (nanocracks) BPN. Results show that, under uniaxial tensile loading, BPN is converted into four distinct morphologies before fracture starts. This conversion process is dependent on the stretching direction. Some of the formed structures contain mainly eight-membered rings, which have different shapes in each morphology. In one of them, a graphitization process occurs before the complete fracture. Importantly, in the presence of nanocracks, no new morphologies are formed. BPN exhibits a distinct fracture process when contrasted to graphene. After the critical strain threshold, the graphene transitions from an elastic to a brittle regime, while BPN can exhibit different inelastic stages. These stages are associated with the appearance of new morphologies. However, BPN shares some of the exceptional graphene properties. BPN Young's modulus and melting point are comparable to graphene, about 1019.4 GPa and 4024 K, respectively.

Received 3rd December 2021,
Accepted 4th February 2022

DOI: 10.1039/d1nr07959j

rsc.li/nanoscale



## 1. Introduction

Since the discovery of graphene,[1] carbon-based 2D systems have attracted considerable attention from the scientific community due to unique properties and potential applications, such as novel energy storage[2–4] and conversion,[5–7] with good efficiency and low environmental impact. They often exhibit a combination of low cost and relatively easy fabrication, yielding different structures.[8–14] These features make carbon-based 2D systems suitable for such a wide range of applications.[15]

The advent of graphene renewed the interest in 2D carbon, and recently other structures have been proposed in the literature, but most of them were not experimentally realized.[16–22] Some of these novel 2D allotropes have the advantage of presenting a non-zero bandgap, which is one of the limiting features of using graphene in a series of optoelectronic applications.

Very recently, a new synthetic route to obtain a graphene-like structure—2D biphenylene network (BPN)[11]—was reported. BPN consists of the periodic arrangement of a set of four, six, and eight carbon rings fused side by side. Armchair-like BPN nanoribbons present similar electronic properties to armchair graphene nanoribbons.[11] In this sense, the 2D layered BPN structure emerges as a promising material and needs further investigation to understand its structural, electronic, and mechanical properties.

When it comes to the synthesis of nanostructures, the presence of defects is a reality.[23] In many cases, such a tendency should not be considered a failure in the process but rather a crucial feature.[24] For instance, defects are known to provide substantial changes in the mobility of charge carriers in otherwise semiconducting systems, such as armchair graphene nanoribbons.[25] Defects are also a reality in organic synthesis. However, to take advantage of possible structural defects, a detailed study of their influence on the system performance is needed.

Due to BPN promising features, there are several theoretical works investigating their structural and electronic properties, most of them carried out before their experimental

[a]*Institute of Physics, University of Brasília, 70910-900 Brasília, Brazil. E-mail: ribeirojr@unb.br*
[b]*Department of Electrical Engineering, University of Brasília 70919-970, Brazil*
[c]*Applied Physics Department, University of Campinas, Campinas, São Paulo, Brazil*
[d]*Center for Computing in Engineering and Sciences, University of Campinas, Campinas, São Paulo, Brazil*

†Electronic supplementary information (ESI) available. See DOI: 10.1039/d1nr07959j

realization.[26–29] These works have addressed different BPN features, such as their electronic structure[30,31] and potential use as a material source for Lithium-ion batteries.[32] Nevertheless, detailed studies of their mechanical properties, and fracture patterns, have not been yet investigated. More specifically, an understanding of the influence of lattice defects (such as cracks/notches) is still missing in the literature.

In this work, we have carried out fully atomistic reactive (Reaxff) molecular dynamics simulations to investigate the mechanical properties of both pristine and defective (with nanocracks/notches) BPN. We were able to map different phase transitions regarding the response of the system structure when subjected to uniaxial strain. We also show that BPN exhibits a quite distinct mechanical behavior when contrasted to graphene. After a critical strain threshold, the graphene sheet goes directly from elastic to brittle regimes, while BPN has different intermediate structural stages. These stages are associated with forming other structures types and (or) linear atomic changes. Interestingly, we found that the calculated BPN Young's modulus value and melting point are comparable to the graphene ones.

## 2. Methodology

We studied the mechanical and thermal properties of non-defective and defective BPN were investigated by employing fully atomistic MD simulations with the reactive force field ReaxFF,[33] as implemented in the large-scale atomic/molecular massively parallel simulator (LAMMPS) code.[34] Importantly, the ReaxFF potential allows the formation and breaking of chemical bonds during the dynamics, which is necessary to investigate the fracture mechanisms.[35] The ReaxFF parameterization for carbon-based systems is modern and has considered density functional theory (DFT)-derived mechanical data for diamond and graphite in the fitting set.[36] In addition, this force field was successfully tested in the calculation of the mechanical properties of diamond, graphene, carbon nanotubes, and amorphous carbon.[36,37] Some studies in the literature have demonstrated that ReaxFF results are comparable to *ab initio* molecular dynamics simulations.[38,39] The BPN studied here are illustrated in Fig. 1. Fig. 1(a, b), (c, d), and (e, f) present the non-defective BPN, a BPN with a horizontally aligned nanocrack, and a BPN with a vertically aligned nanocrack, respectively.

In Fig. 1, the bottom sequence of panels shows zoomed regions of the corresponding lattices. We used BPN structural models with dimensions of 96.56 × 95.58 Å$^2$ with the atoms at the edges fixed to avoid spurious effects during the stretching processes. The BPN thickness is 3.5 Å (one atom thickness). We did not use periodic boundary conditions. We fixed approximately 15 Å of each edge along the $x$-direction (left and right edges) and $y$-direction (top and bottom edges) of model BPN. In this way, we simulated the uniaxial tensile loading by moving the edges in the opposite direction with a constant strain rate. The horizontally and vertically aligned nanocracks have dimensions of 23.30 × 5.70 Å$^2$ and 27.00 × 5.30 Å$^2$, respectively. The total number of carbon atoms is 3450 for the non-defective case, 3414 for the horizontal nanocrack, and 3416 for the vertical nanocrack, respectively. It is worthwhile mentioning that BPN bond lengths $I_1$ = 1.45 Å, $I_2$ = 1.46 Å, and $I_3$ = 1.41 Å (as stands ref. 40) presented in the literature by employing density functional theory calculations[31,40] are similar to the bond lengths obtained in the present work (after energy minimization), that are 1.43 Å, 1.47 Å, and 1.39 Å, respectively. We would like to stress that the good agreement of the bond-length values between ReaxFF and DFT, as well as, with the general trends of the elastic properties with AIREBO (see Table S1 of the ESI†), shows that ReaxFF is an appropriate force field choice for our problem.

We numerically integrated the equations of motion using the velocity-Verlet integrator with a time-step of 0.05 fs. The

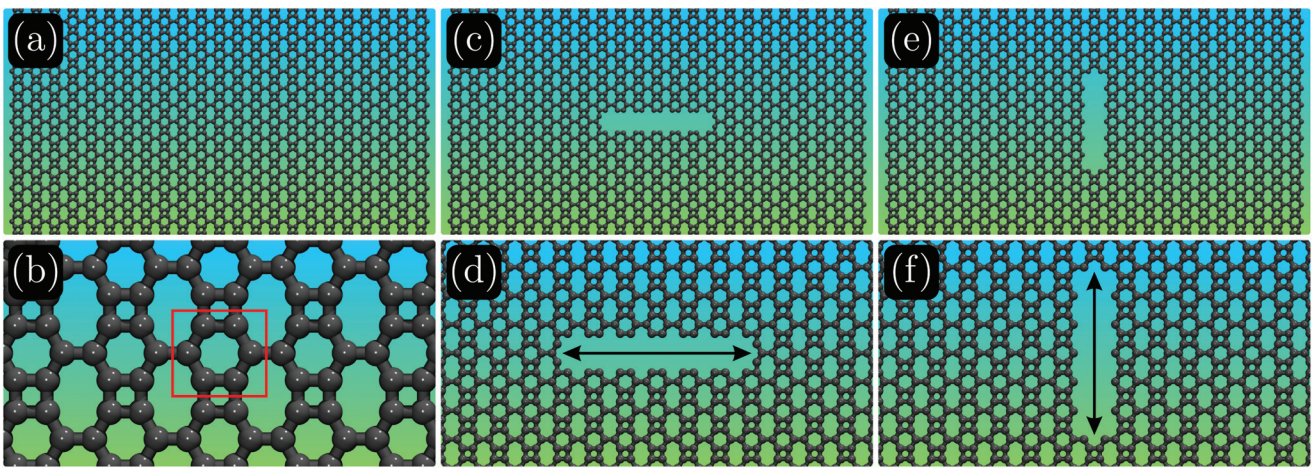


**Fig. 1** Schematic representation of the BPN structures studied here: (a and b) non-defective BPN, (c and d) a BPN with a horizontally aligned nanocrack ($x$-direction), and (e and f) a BPN with a vertically aligned nanocrack ($y$-direction). The bottom sequence of panels shows zoomed regions of the corresponding lattices. The red rectangle in panel (b) represents the asymmetric unity cell.

tensile stress was applied considering a uniaxial strain along with the non-periodic $x$ and $y$ directions, for an engineering strain rate of $1.0 \times 10^{-6}$ fs$^{-1}$. Before the BPN stretching, the structures were equilibrated within an NPT ensemble at a constant temperature of 300 K and null pressures using a Nosé–Hoover thermostat[41] during 200 ps. More details about this methodological approach can be found in the ref. 42.

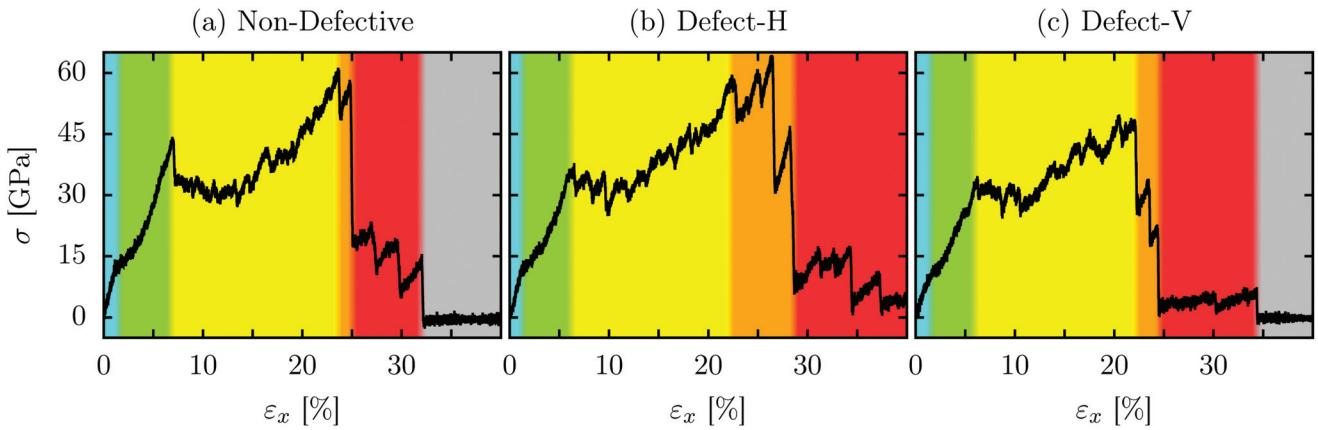


Fig. 2 Stress–strain curves (for strain applied along the $x$-direction) for: (a) non-defective, (b) horizontally defective (Defect-H), and (c) vertically defective (Defect-V) BPN.

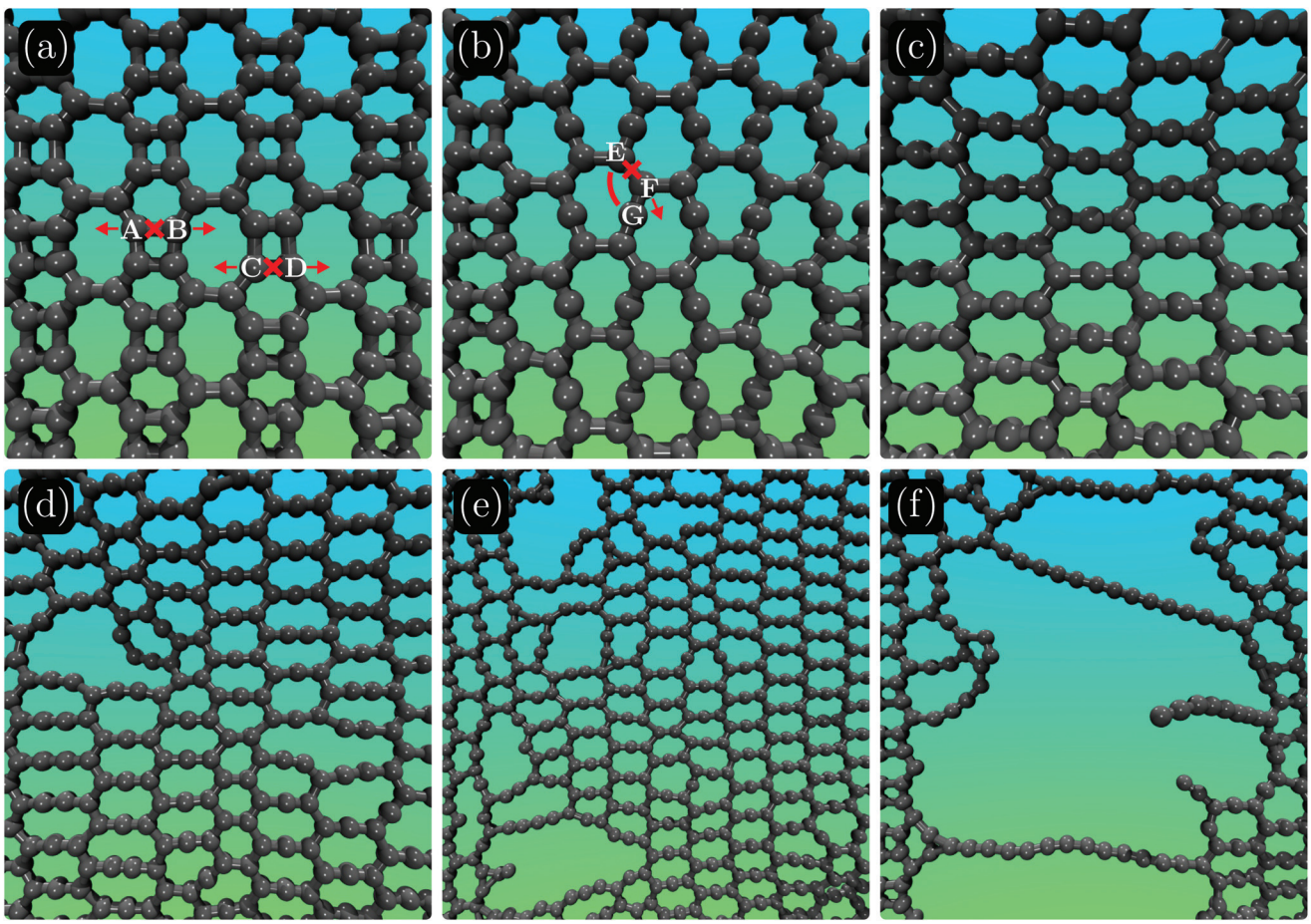


Fig. 3 Representative MD snapshots of the BPN at different strain values (applied along the $x$-direction, $\varepsilon_x$) for the non-defective case. The panels in this figure represent the following strain percentages: (a) 0%, (b) 5%, (c) 20%, (d) 23%, (e) 28%, and (f) 30%. See text for discussions.

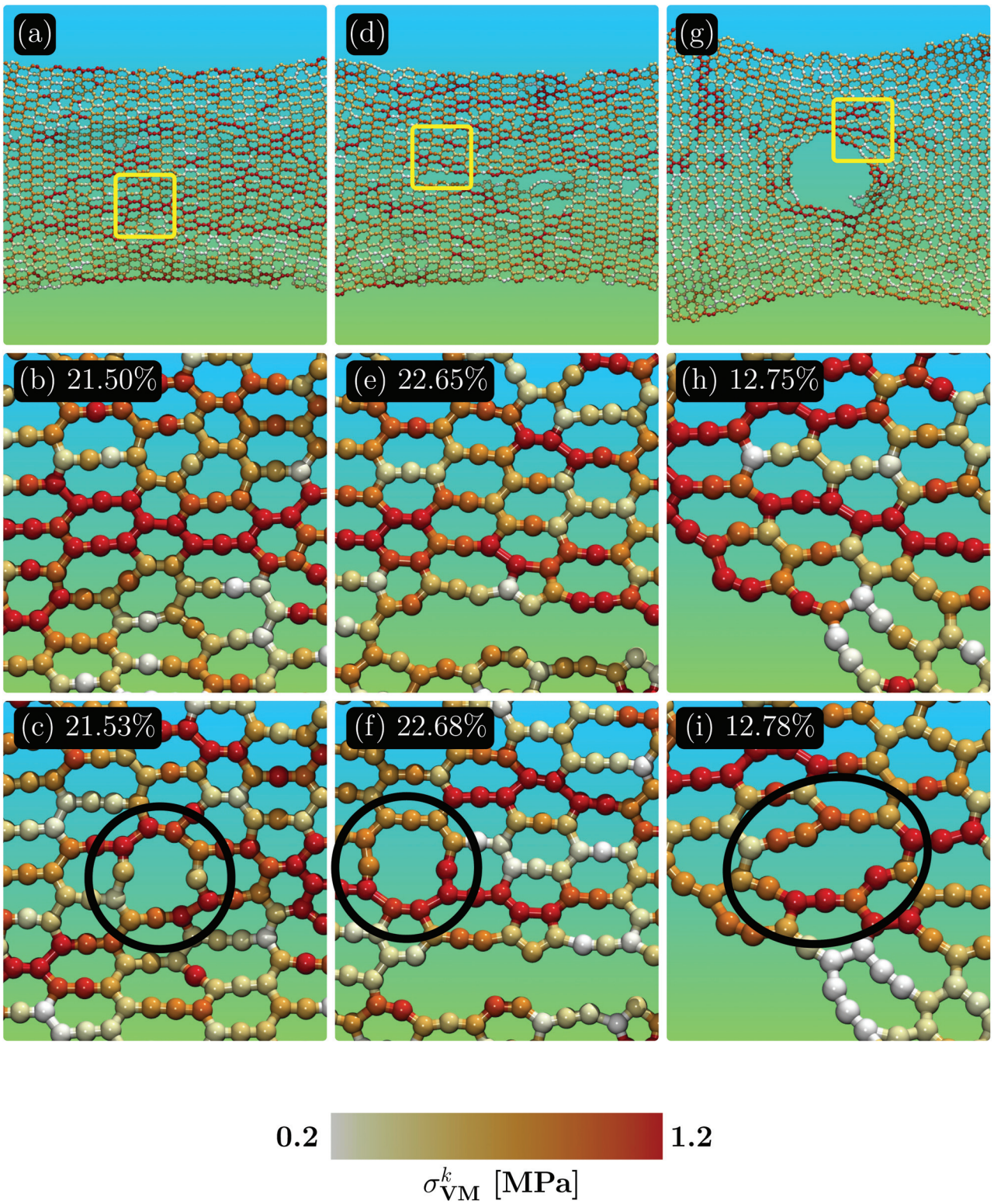


**Fig. 4** Representative MD snapshots with the von Mises stress ($\sigma^k_{\mathrm{VM}}$) per-atom values for the BPN under a tensile loading applied along the *x*-direction. (a–c), (d and e), and (g–i) present the $\sigma^k_{\mathrm{VM}}$ distribution for the non-defective BPN (at 21.50% and 21.53% of strain before and after the fracture, respectively), Defect-H BPN (at 22.65% and 22.68% of strain before and after fracture, respectively), and Defect-V BPN (at 12.75% and 12.78% of strain before and after the fracture, respectively), respectively. The top sequence of panels shows a general view of the BPN cases for the time step before their first fracture regime. The middle sequence of panels is the zoomed regions indicated by the yellow squares. These regions show the first bond breaking for each case. The bottom sequence of panels illustrates the bond reconstructions and the newly formed rings (black circles) after the first bond-breaking cycle.

The BPN structures shown in Fig. 1 were continuously stretched up to their complete structural failure (fracture), which can be identified by the fractured and irreversible patterns presented by the lattices and by the abrupt change in the stress values. The maximum applied strain was 50%. We calculated the von Mises stress (VM) per-atom values.[43] These values provide information on the fracture process once they reveal the fracture point or region. More details about the VM calculations can be found in the LAMMPS manuals[44] and in ref. 42. Using this MD simulation scheme, we obtained the following elastic properties from the stress–strain curves: Young's modulus ($Y_M$), Fracture Strain (FS), and Ultimate Strength (US). We also calculate the stress intensity factor (SIF), which is a fracture parameter that measures the stress intensity near the tip of the crack[45] and can be defined as $K_I = \sigma_{DD}\sqrt{2\pi r_D}$, where $D$ stands for $x$ or $y$. In this equation, $r_D$ is the nanocrack length in the direction of the applied strain, and $\sigma_{DD}$ is the stress distribution along the $D$ direction. The MD snapshots and trajectories were obtained using the visualization and analysis software VMD.[46]

## 3. Results

We begin our discussion by investigating the stress ($\sigma$) response as a function of the $x$-direction applied strain ($\varepsilon_x$), as illustrated in Fig. 2. The $x$-strain corresponds to the horizontal direction in Fig. 1, *i.e.*, parallel to the nanocrack of Fig. 1(d). The following observations are valid for the three represented systems. As we can see from this figure, as the strain increases, the unstressed regime (cyan regions) of the BPNis followed by the green and yellow regions, respectively. These regions are related to the elastic regime and the first and second inelastic regimes, respectively. A further stress increase yields a new lattice configuration corresponding to the orange region. This region is associated with the beginning of the structural failure (fracture) process. Ultimately, linear atomic chains (LACs) are formed until the complete BPN fracture (red regions). Completely fractured lattices are in the gray region, in which the stress value drops to zero.

The three panels of Fig. 2 represent the behavior of BPN with different structures: 2(a) the non-defective structure, 2(b) the structure with a horizontal nanocrack defect (Defect-H), and 2(c) the structure with a vertical nanocrack defect (Defect-V). Although the structural fracture process starts approximately at the same strain values, the process as a whole is distinct. The nanocrack leads to the appearance of more resilient LACs, as can be seen from the broadening of the red regions of Fig. 2(b) and (c), when compared to Fig. 2(a). The complete fracture now occurs at higher strain values. Interestingly, the Defect-H case is the most resilient, as discussed later.

Fig. 3(a–f) show representative MD snapshots for the strain applied along the horizontal direction ($\varepsilon_x$) for the non-defective case. In the ESI,† we present the video for this MD simulation (see video1.mpg). Fig. 3(a) shows that, in the initial stages of the process, the A and B type atoms begin to have their mutual bonds dissociated, thus causing the first phase transition in the lattice structure. As the strain increases, the E-Gatoms come closer together, which leads to a bond formed between them. As a result, this further weakens the bonds between the E and F atoms, thus starting the new phase of the inelastic regime. We observed that each new-formed phase is less stressed than the previous one: the structure as a whole is structurally softened. This trend occurs because as $\varepsilon_x$ increases, the porosity of the structure increases as vacancy defects resulting from the new bond pattern appears, as illustrated in Fig. 3(d). The starting of the structural failure (fracture) is shown in Fig. 3(e), it further continues in Fig. 3(f) with the LAC formation until the BPN is completely fractured.

To better discuss the BPN dynamics under a tensile loading applied along the $x$-direction, we present in Fig. 4 representative MD snapshots with the von Mises stress ($\sigma^k_{VM}$) per-atom values.[42,43] The ($\sigma^k_{VM}$) values provide local structural information on the fracture process since they can indicate the regions from which the fracture starts. In this way, Fig. 4(a–c), (d, e), and (g–i) present the $\sigma^k_{VM}$ distribution for the non-defective BPN (at 21.50% and 21.53% of strain before and after the fracture, respectively), Defect-H BPN (at 22.65% and 22.68% of strain before and after fracture, respectively), and Defect-V BPN (at 12.75% and 12.78% of strain before and after the fracture, respectively). Such values for the fracture strain stand that the vertical defect weakens the lattice. The top sequence of panels shows an overview of BPN cases for a time step before their first fracture. The middle sequence of panels shows the regions within the yellow squares for their corresponding cases, which were zoomed for clarity. These regions show the first bond breaking for each case. The bottom sequence of panels illustrates the bond reconstructions and the newly formed rings (black circles) after the first bond breaking.

In Fig. 4(a–c) and (d–f) we can see that $\sigma^k_{VM}$ tends to accumulate in the carbon–carbon bonds almost parallel to the direction of the applied strain, as can be inferred from the bonds in red in Fig. 4(a) and (d). As a consequence, the bonds parallel to the strain direction that connect the two eight-membered rings (*i.e.*, the bonds belonging to the rings with six atoms) are the first ones to break (see Fig. 4(b) and (e)). After the first bond breaking, bond reconstructions lead to the for-

**Table 1** Elastic properties—Young's modulus ($Y_M$), fracture strain (FS), and ultimate strength (US)—obtained by fitting the stress–strain curves (Fig. 2e and 5) for the Biphenylene Network cases investigated here

| $\sigma_x$ | | | $\sigma_y$ | | |
|---|---|---|---|---|---|
| $Y_M$ [GPa] | FS [%] | US [GPa] | $Y_M$ [GPa] | FS [%] | US [GPa] |
| Non-defective | | | | | |
| 1019.4 | 24.9 | 61.3 | 745.5 | 6.7 | 61.0 |
| Defective-H | | | | | |
| 986.2 | 26.6 | 64.4 | 570.9 | 7.3 | 46.9 |
| Defective-V | | | | | |
| 760.7 | 22.3 | 49.8 | 693.1 | 7.9 | 60.3 |

mation of new rings (or pores) connecting 11 carbon atoms, as highlighted by the black circles in Fig. 4(c) and (f). The bond-breaking (reconstruction) mechanisms occur in several regions of the structure simultaneously. In the ESI,† we present the videos for this MD simulation (see video1.mpg and video2.mpg).

In the case of Defect-H BPN, the nanocrack is aligned to the direction of the applied strain. During the stretching process,

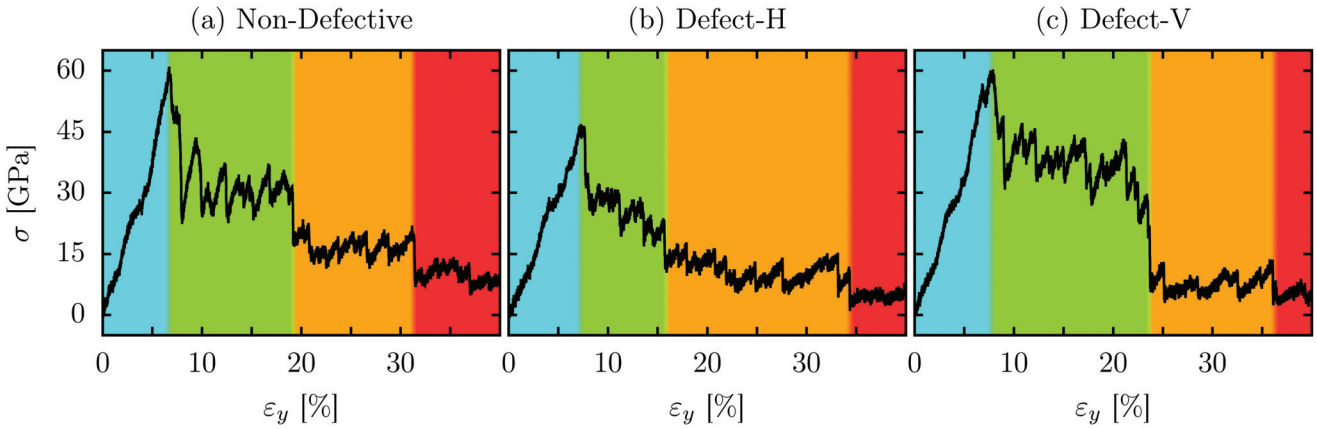


**Fig. 5** Stress–strain curves (for strain applied along the *y*-direction) relation for: (a) non-defective, (b) horizontally defective (Defect-H), and (c) vertically defective (Defect-V) BPNs.

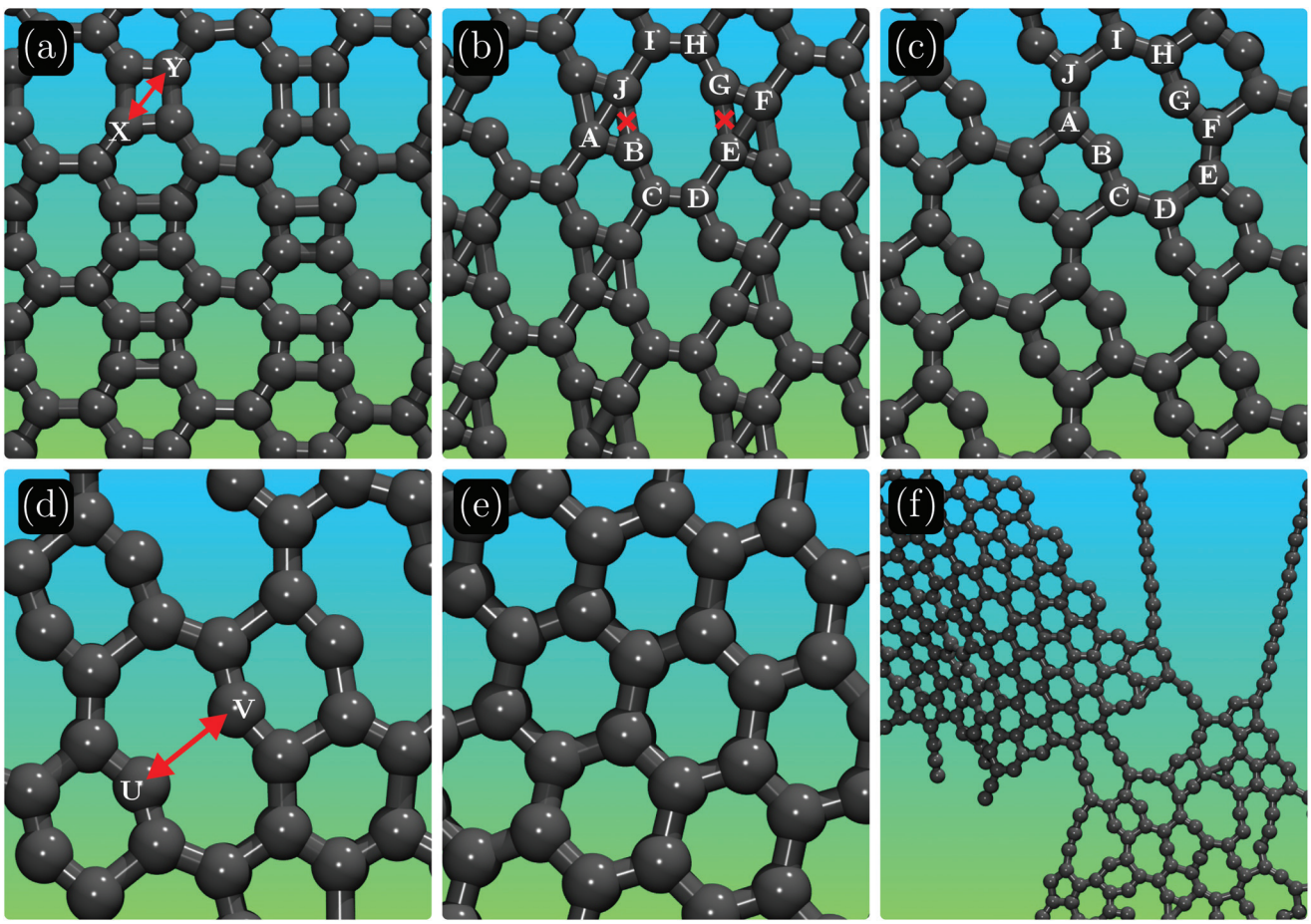


**Fig. 6** Representative MD snapshots of the BPN at different strain values (applied along the *y*-direction, ($\varepsilon_y$)) for the non-defective case. The panels in this figure represent the following strain percentages: (a) 0%, (b) 7%, (c) 8%, (d) 10%, (e) 20%, and (f) 25%. See text for discussions.

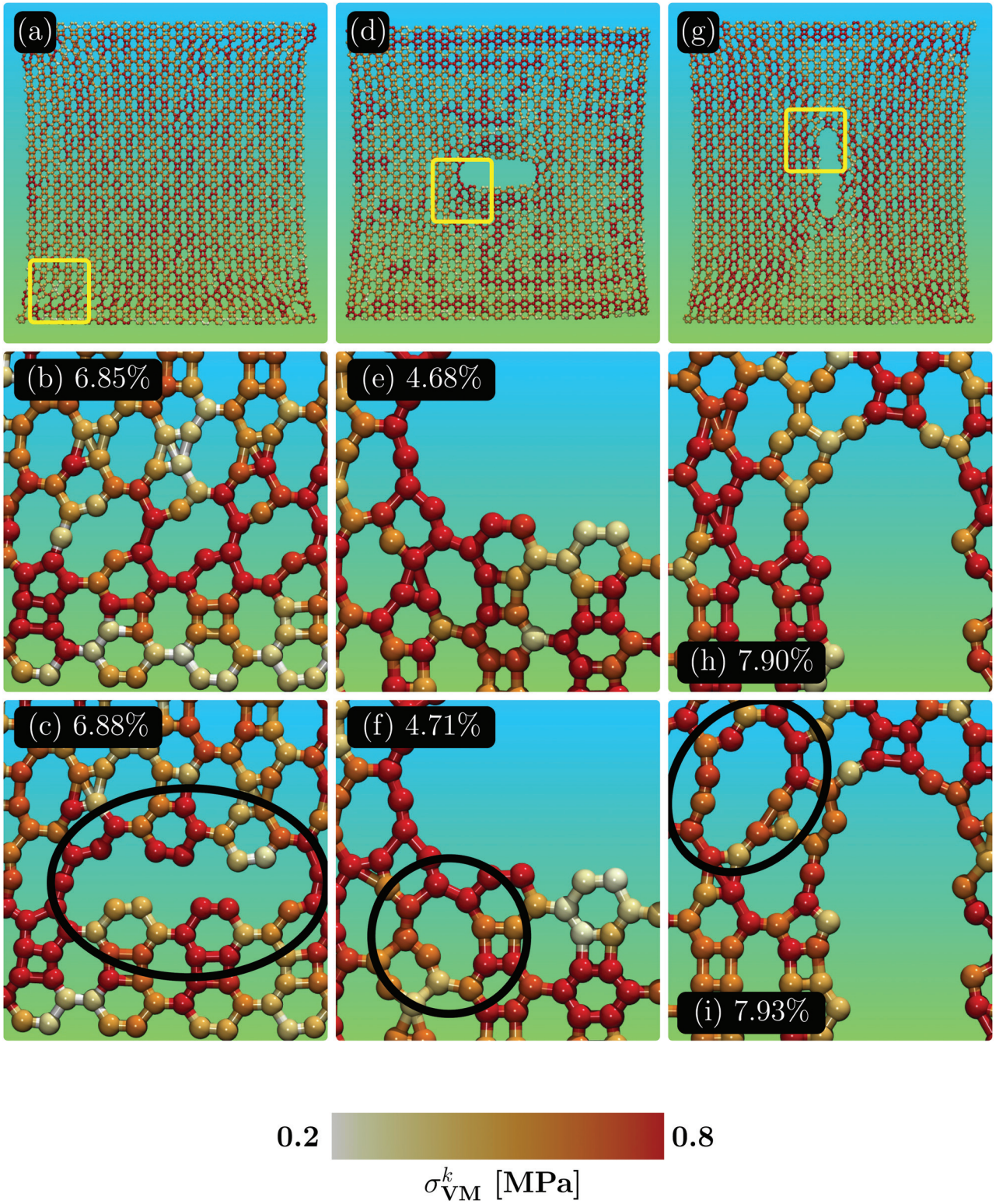


**Fig. 7** Representative MD snapshots with the von Mises stress ($\sigma^k_{\mathrm{VM}}$) per-atom values for the BPN under a tensile loading applied along the *y*-direction. Fig. 4(a–c), (d and e), and (g–i) present the $\sigma^k_{\mathrm{VM}}$ distribution for the non-defective BPN (at 6.85% and 6.88% of strain before and after the fracture, respectively), Defect-H BPN (at 4.68% and 4.71% of strain before and after the fracture, respectively), and Defect-V BPN (at 7.90% and 7.93% of strain before and after the fracture, respectively). The top sequence of panels shows a general view of the BPN cases for the time step before their first fracture regime. The middle sequence of panels is the zoomed regions indicated by the yellow squares. These regions show the first bond breaking for each case. The bottom sequence of panels illustrates the bond reconstructions and the newly formed rings (black circles) after the first bond-breaking cycle.

the atoms nearby the defect come closer when the strain percentage increases. Such a process allows bond reconstructions within the nanocrack, reinforcing the lattice. This process is responsible for the similar behavior presented by the stress–strain curves in Fig. 2(a) and (b). When the nanocrack is oriented perpendicularly to the direction of the applied strain, the non-defective and defective curves are substantially distinct. As expected for this case (*i.e.*, when the nanocrack is aligned perpendicularly to the direction of the tensile loading), the presence of the nanocrack makes the BPN fragile, reducing its Ultimate Strength and Young's modulus, as presented in Table 1. One can also note that the fracture strain of both BPN and graphene monolayers tend to be not sensitive to the presence of a nanocrack when it is aligned in parallel to the stretching direction.[47] When the nanocrack is perpendicularly aligned (Defect-V BPN), most of the bonds that accumulate stress are parallel to the strain direction, as shown in Fig. 4(g–i). The vertical nanocrack leads to an almost uniform distribution of the accumulated stress, and the Defect-H BPN has only a small number of bonds in red (see Fig. 4(g)). In this case, the first bonds to break are the ones nearby the nanocrack (see Fig. 4(h)). The bonds that connect two eight-membered rings side-by-side are the first to break, yielding a pore composed of 13 carbon atoms. In all the cases, the first bond-breaking results in an abrupt fracture followed by fast crack propagation.

In the ESI,† we present videos for an overall visualization of the whole fracture process of these cases (see video1.mpg, video2.mpg, and video3.mpg). In these videos, we can see that the nanocracks preclude the above-mentioned BPN phase transitions.

We now analyze the stress ($\sigma$) response as a function of the strain applied along the $y$-direction ($\varepsilon_y$), as shown in Fig. 5. In the ESI,† we present the video for this MD simulation (see video4.mpg). In this case, the strain is along the vertical direction, parallel to the vacancy defect of Fig. 1(f). Four phases are identifiable from Fig. 5(a), (b), and (c) which, again, correspond to the non-defective, horizontally defective (Defect-H), and vertically defective (Detect-V) BPN, respectively. The cyan region corresponds to the non-stressed structure. At the end of this region, a phase transition process leads to the beginning of the structural failure. Green and orange regions correspond to the continuing of such a process. In red, the formation of LACs takes place, followed by the completely fractured structure (the null stress grey regions in Fig. 2, not shown in Fig. 5). In all the cases, the fracture occurs at approximately the same range between 7 and 8% of strain. The horizontal defect in Fig. 5(b) leads to an increased softened structure, which results in a slightly smaller Ultimate Stress value when compared to the other cases (about 15 GPa of difference). We can see that the vertical defect results in an increase in the structural strength.

In Fig. 6 we present representative MD snapshots that illustrate the fracture mechanism corresponding to the process described in Fig. 5. In Fig. 6(a), we can see that atoms X and Y become closely bonded. From Fig. 6(b), we observe that the J–B and the G–E pairs begin to dissociate, thus starting a new phase shown in Fig. 6(c). Such a bond reconfiguration trend appears in several parts of the structure easing the fracture process in some (but not all) of those parts. In the cases that such fracture does not take place, the U and V atoms of Fig. 6(d) come closer to one other, thus creating a local graphene-type structure. This new rearrangement takes place in several regions of the structure. The system tends to become increasingly more similar to graphene, as can be seen in Fig. 6(e). In Fig. 6(f), we can observe larger pores, more graphene-type regions, and the appearance of LACs that precedes the complete fracture. Because of this dynamical behavior, this fracture pattern can be described as a *tearing-like process.*[48]

In Fig. 7 we present representative MD snapshots with ($\sigma^{k}_{VM}$) per-atom values for the cases that consider the strain applied along the $y$-direction. In Fig. 7(a–c), (d–f), and (g–i) we present the $\sigma^{k}_{VM}$ distribution for the non-defective BPN (at 6.85% and 6.88% of strain before and after the fracture, respectively), Defect-H BPN (at 4.68% and 4.71% of strain before and after the fracture, respectively), and Defect-V BPN (at 7.90% and 7.93% of strain before and after the fracture, respectively). This Figure has the same layout used in Fig. 4. In the ESI,† we present videos for an overall visualization of the whole fracture process of the cases mentioned above(see video4.mpg for the non-defective case, video5.mpg for the Defect-H case, and video6.mpg for the Defect-V case, respectively).

Unlike the cases of Fig. 4, we observe a tendency for stress accumulation into the four- and six-membered rings (see Fig. 7(a, d and g)), but not necessarily in the bonds aligned to the direction of the applied strain. This tendency disappears when the critical strain value is reached, as a result of the morphological changes (see Fig. 7(b, e and h)). For all cases, BPN presents a significant fracture strain value when contrasted to the systems shown in Fig. 4. This trend is because, in this

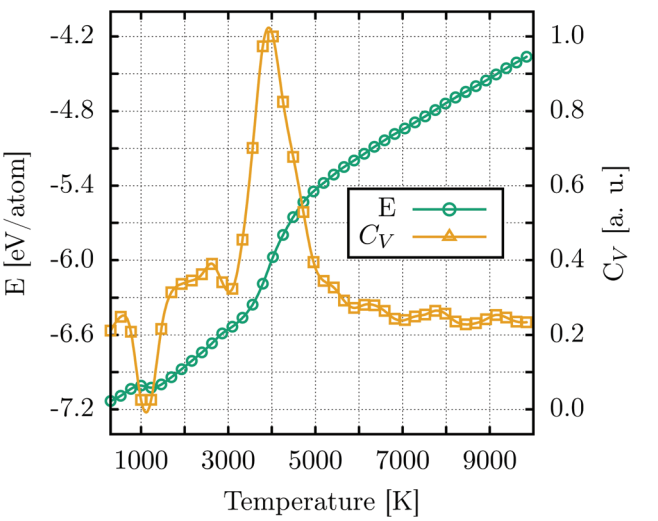


**Fig. 8** BPN total energy and heat capacity ($C_V$) as a function of temperature for the 250 ps heating ramp simulations (melting process).

stretching mode, the bond-break forms large pores, resembling nanocracks (see Fig. 7(c)) or they broke near the nanocrack (see Fig. 7(f) and (i)), which is the most fragile structural region.

The numeric values of the elastic properties are presented in Table 1. The Young's Modulus ($Y_M$) values were calculated using a linear fitting of the stress within the first 1% of strain. The Fracture Strain (FS) is obtained from the strain percentage corresponding to the largest stress value, *i.e.*, the Ultimate Strength (US). We can see that the fracture strain for the non-defective structure (24.9%) lies between the ones for the Defect-H (26.6%) and Defect-V (22.3%) BPN when the strain is applied along the *x*-direction. Considering the strain applied along the *y*-direction, the non-defective BPN presented the smallest FS (about 6.7%). The values obtained for the stress intensity factor (SIF) related to the defect-H (*x*-direction), defect-V (*x*-direction), defect-H (*y*-direction), defect-V (*y*-direction) are 7.3, 2.8, 2.7, and $7.9 \times 10^6$ Pa $\sqrt{m}$, respectively.

Importantly, when the tensile loading direction is perpendicular to the nanocrack, this defect plays the role of softening the structure. The US values for Defective-V under $\varepsilon_x$ and Defective-H under $\varepsilon_y$ are 49.8 GPa and 46.9 GPa, respectively. They are the smallest values among all the structures within the same simulation protocol. On the other hand, in the simulations in which the tensile loading direction is parallel to the nanocrack, this defect increases (or does not substantially affect) the BPN resilience to tension. The US values for Defective-H under $\varepsilon_x$ and Defective-V under $\varepsilon_y$ are 64.4 GPa and 60.3 GPa, respectively. When the nanocrack is parallel to the stretching direction, the distance between the atoms at the edge of this defect decreases when the strain increases, allowing bond reconstructions within the defective region.

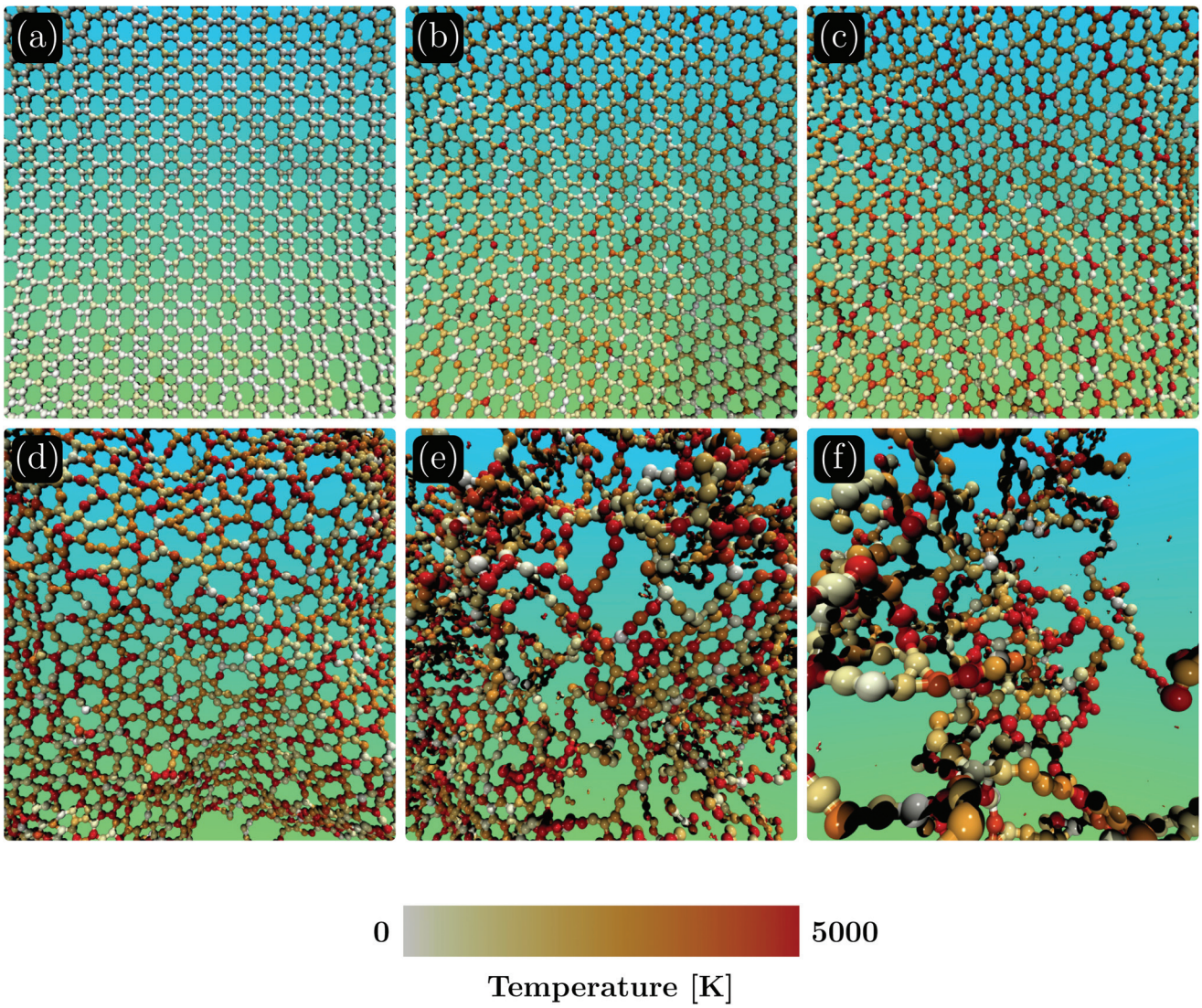


**Fig. 9** Representative MD snapshots for the heating ramp simulations (melting process). The color scale indicated the temperature per atom ranging from 300 K (white) to 5000 K (red). (a) 300 K at 5 ps, (b) 1000 K at 5 ps, (c) 2000 K at 50 ps, (d) 3000 K at 75 ps, (e) 4000 K at 100 ps, and (f) 5000 K at 125 ps.

These bond reconstructions are responsible for increasing the BPN US value with the nanocrack. We obtained $Y_M$ values ranging from 570.9 to 1019.4 GPa. These values are comparable to the Young's modulus of graphene, obtained through density functional theory, molecular dynamics simulations, continuum models, and finite element methods (between 698.0 and 1367 GPa),[30,49,50] consistent with the experiments values, which varies from 890 GPa (ref. 51) up to 1000 GPa.[52] For the sake of comparison, the $Y_M$ of boron nitride (hBN) and molybdenum disulfide ($MoS_2$) sheets are ≈865 GPa (ref. 53) and ≈330 GPa,[54] respectively. Note that these values are close to the $Y_M$ value obtained here for BPN.

Finally, we analyzed the BPN thermal stability. First, we carried out heating ramp simulations (melting process), with temperatures varying from 300 K to 10 000 K during 250 ps. Fig. 8 illustrates the total energy (green) and heat capacity (yellow) as a function of temperature for the melting process of BPN. From this figure, we can see that the total energy increases quasi-linearly with the temperature with three different regimes well-defined by the different slopes in Fig. 8: between 300 K–1000 K, 1100 K–3900 K, and 5000 K–10 000 K. Note that the melting point definition refers to the initial structure and its sublimation temperature.

In the first heating regime (up to 850 K), BPN still maintains its structural integrity. Between 850–1100 K, the thermal vibrations lead to considerable changes in the original BPN morphology, and the first phase transition takes place, resulting in a structure similar to the one presented in Fig. 3(b). This structural phase transition is characterized by the first peak (discontinuity in the $C_V$) and the total energy curves, respectively. The second heating regime (between 1100 K–3900 K) is associated with continuous heating up of the newly formed configuration. The BPN melting takes place between 3900 K–5000 K. In this temperature interval, we can see the appearance of a well-pronounced peak in the $C_V$ curve and a discontinuity in the total energy curve that is related to a phase transition from a solid to a gas-like phase. The BPN melting point occurs at 4024 K, which is represented by the well-pronounced peak in the $C_V$ curve. This value is comparable to the melting point for the monolayer graphene (4095 K) and the amorphous monolayer graphene (3626 K).[55] Previous works have also predicted a melting point for graphene between 4000 K and 6000 K.[56–58]

The complete BPN melting takes place at around 5000 K. Up to this critical value, the total energy curve does not show changes in the slope. The slope change observed between 3900 K–5000 K is related to a gain in kinetic energy due to the higher atom velocities in the gas-like phase. Harmonic and torsional energies are converted into kinetic energy in the solid phase during the melting process. This process contributes to the increase in the total energy value. Above 5000 K, the gas-phase dominates, characterizing the third heating regime between 5000 K–10 000 K.

In Fig. 9 we present representative MD snapshots for the heating ramp simulations, with temperature varying from 300 K up to 5000 K, as previously described. The color scheme denotes the temperature per atom ranging from 300 K (white) to 5000 K (red). At low temperatures (up to 300 K), BPN presents a morphology very similar to the one of minimum energy, as illustrated in Fig. 9(a) for 300 K. At 1000 K (see Fig. 9(b) and (c)), the thermal fluctuations induce changes in the morphology, as mentioned above. The resulting structures are similar to the one presented in Fig. 3(b). In this sense, temperature and strain have a similar impact on the structural changes at low-temperature regimes. At 3000 K, the melting process of the lattice starts to occur, as illustrated in Fig. 9(d). In this figure, one can observe that the temperature effects also induce a graphitization process. Above 4000 K, the thermal vibrations favor the formation of LACs, and no BPN fragments can be observed, as shown in Fig. 9(a). For temperatures about 5000 K, only isolated atoms and small LACs are observed, and the state at the end of the heating ramp simulation is a gas-like phase.

## 4. Summary and conclusions

We have carried out fully atomistic reactive (ReaxFF) molecular dynamics (MD) simulations to investigate the mechanical stability and fracture dynamics of non-defective and defective (differently oriented nanocracks, vertically/Defect-V and horizontally/Defect-H oriented) 2D biphenylene networks (BPN), which was recently synthesized.[11] Our results showed that, under uniaxial tensile loading, BPN is converted into distinct morphologies before its complete structural failure (fracture). As the strain increases, three different phases in the inelastic regimes were formed. When the critical strain (fracture strain) is reached, and the fracture process starts, linear atomic chains (LAC) are formed until BPN is completely fractured.

In one of the observed inelastic regimes, a graphitization (structural transformation to graphene-like structure) process occurs before the BPN complete fracture. In the presence of nanocracks, no new structure is formed (*i.e.*, there is no formation of distinct elastic regimes). The fracture strains obtained here were 24.9% (6.7%), 26.6% (7.3%), and 22.3% (7.9%) for the non-defective BPN, Defect-H, and Defect-V, respectively, considering the strain applied along the *x*-direction (*y*-direction). The vertical defect weakens the lattice. In the case of Defect-H, the nanocrack is aligned to the direction of the applied strain. During the stretching process, the atoms within the defective region come closer when the strain rate is increased. This process allows bond reconstructions within the nanocrack, which are responsible for slightly increasing the strain rate experienced by the BPN structure for this case when contrasted to the non-defective one.

Unlike the cases where the strain was applied along the *x*-direction, for the *y*-direction tensile loading, there is a tendency for stress accumulation in the four- and six-membered carbon rings, but not necessarily in the bonds aligned to the direction of the applied strain. This tendency disappears when BPN achieves its critical strain because of the morphological changes induced by the applied stress. The BPN, when

stretched along the *y*-direction, presents the lower fracture strain. For the *y*-direction stretching, the bonds break by forming large pores, resembling new nanocracks, or they break near the initial nanocrack, which is the most fragile structural region.

BPN exhibits distinct fracture dynamics when contrasted to graphene. After the critical strain threshold, graphene directly transitions from an elastic to a brittle regime,[55] while BPN exhibits different deformable stages. As mentioned above, these stages are associated with the formation of other structural morphologies.

We obtained Young's modulus values ranging from 570.9 to 1019.4 GPa. These values are comparable to graphene values, obtained from other theoretical works (between 698.0 and 1367 GPa),[30,49,50] and are consistent with the experimental values, which varies from 890 GPa (ref. 51) up to 1000 GPa.[52] From the heating simulations, we obtained a melting point of 4024 K for BPN. This value is comparable to the one for pristine (4095 K) and amorphous graphene (3626 K).[55] Previous works have also predicted a melting point for graphene between 4000 K and 6000 K.[56–58] The BPN complete melting was observed around 5000 K.

The recently reported BPN synthesis[11] opens new and exciting perspectives for 2D carbon-based materials. BPN shares some of the exceptional graphene properties. We hope the present work will stimulate further BPN investigations.

## Conflicts of interest

There are no conflicts to declare.

## Acknowledgements

The authors gratefully acknowledge the financial support from Brazilian research agencies CNPq, FAPESP, and FAP-DF. M. L. P. J gratefully acknowledges the financial support from CAPES grant 88882.383674/2019-01. L. A. R. J acknowledges the financial support from a Brazilian Research Council FAP-DF grants 00193-00000853/2021-28 and 00193-00000811/2021-97 and CNPq grant 302236/2018-0, respectively. L. A. R. J acknowledges CENAPAD-SP for providing the computational facilities. L. A. R. J. gratefully acknowledges the financial support from IFD/UnB (Edital 01/2020) grant 23106.090790/2020-86. W. F. C. acknowledges the financial support from FAPDF grant 00193-00000857/2021-14. The authors acknowledge the National Laboratory for Scientific Computing (LNCC/MCTI, Brazil) for providing HPC resources of the SDumont supercomputer, which have contributed to the research results reported within this paper. URL: http://sdumont.lncc.br.DSG acknowledges the Center for Computational Engineering and Sciences at Unicamp for financial support through the FAPESP/CEPID Grant #2013/08293-7. L. A. R. J. and R. T. S. J. gratefully acknowledge the support from ABIN grant 08/2019. R. T. S. J. gratefully acknowledges, respectively, the support from EC Horizon 2020 HEROES project grant 101021801, CNPq grants 465741/2014-2 and 312180/2019-5, CAPES grant 88887.144009/2017-00, and FAP-DF grants 0193.001366/2016 and 0193.001365/2016.

## References

1 A. K. Geim and K. S. Novoselov, *Nanoscience and technology: a collection of reviews from nature journals*, World Scientific, 2010, pp. 11–19.
2 Q. Ma, Y. Yu, M. Sindoro, A. G. Fane, R. Wang and H. Zhang, *Adv. Mater.*, 2017, **29**, 1605361.
3 L. Miao, Z. Song, D. Zhu, L. Li, L. Gan and M. Liu, *Mater. Adv.*, 2020, **1**, 945–966.
4 H. Geng, Y. Peng, L. Qu, H. Zhang and M. Wu, *Adv. Energy Mater.*, 2020, **10**, 1903030.
5 Y. Zheng, Y. Jiao and S. Z. Qiao, *Adv. Mater.*, 2015, **27**, 5372–5378.
6 S. T. Latibari and S. M. Sadrameli, *Sol. Energy*, 2018, **170**, 1130–1161.
7 J. Zhang, Z. Xia and L. Dai, *Sci. Adv.*, 2015, **1**, e1500564.
8 R. Kumar, E. Joanni, R. K. Singh, D. P. Singh and S. A. Moshkalev, *Prog. Energy Combust. Sci.*, 2018, **67**, 115–157.
9 K. S. Novoselov, V. Fal, L. Colombo, P. Gellert, M. Schwab, K. Kim, *et al.*, *Nature*, 2012, **490**, 192–200.
10 D. Li and R. B. Kaner, *Science*, 2008, **320**, 1170–1171.
11 Q. Fan, L. Yan, M. W. Tripp, O. Krejčí, S. Dimosthenous, S. R. Kachel, M. Chen, A. S. Foster, U. Koert, P. Liljeroth, *et al.*, *Science*, 2021, **372**, 852–856.
12 C.-T. Toh, H. Zhang, J. Lin, A. S. Mayorov, Y.-P. Wang, C. M. Orofeo, D. B. Ferry, H. Andersen, N. Kakenov, Z. Guo, *et al.*, *Nature*, 2020, **577**, 199–203.
13 S. Schmidt, G. Greczynski, C. Goyenola, G. K. Gueorguiev, Z. Czigány, J. Jensen, I. G. Ivanov and L. Hultman, *Surf. Coat. Technol.*, 2011, **206**, 646–653.
14 G. K. Gueorguiev, Z. Czigány, A. Furlan, S. Stafström and L. Hultman, *Chem. Phys. Lett.*, 2011, **501**, 400–403.
15 X. Liu and L. Dai, *Nat. Rev. Mater.*, 2016, **1**, 1–12.
16 A. N. Enyashin and A. L. Ivanovskii, *Phys. Status Solidi B*, 2011, **248**, 1879–1883.
17 S. Zhang, J. Zhou, Q. Wang, X. Chen, Y. Kawazoe and P. Jena, *Proc. Natl. Acad. Sci. U. S. A.*, 2015, **112**, 2372–2377.
18 Z. Wang, X.-F. Zhou, X. Zhang, Q. Zhu, H. Dong, M. Zhao and A. R. Oganov, *Nano Lett.*, 2015, **15**, 6182–6186.
19 X. Li, Q. Wang and P. Jena, *J. Phys. Chem. Lett.*, 2017, **8**, 3234–3241.
20 S. Wang, B. Yang, H. Chen and E. Ruckenstein, *J. Mater. Chem. A*, 2018, **6**, 6815–6821.
21 Z. Zhuo, X. Wu and J. Yang, *Nanoscale*, 2020, **12**, 19359–19366.
22 X. Chen, A. Bouhon, L. Li, F. M. Peeters and B. Sanyal, *Carbon*, 2020, **170**, 477–486.
23 H. Gleiter, *Adv. Mater.*, 1992, **4**, 474–481.

 

24 Z. Fang, B. Bueken, D. E. De Vos and R. A. Fischer, *Angew. Chem., Int. Ed.*, 2015, **54**, 7234–7254.
25 W. F. da Cunha, L. A. Ribeiro, A. L. de Almeida Fonseca, R. Gargano and G. M. e Silva, *Carbon*, 2015, **91**, 171–177.
26 M. R. Hosseini, R. Esfandiarpour, S. Taghipour and F. Badalkhani-Khamseh, *Chem. Phys. Lett.*, 2020, **754**, 137712.
27 R. Esfandiarpour, M. R. Hosseini, N. L. Hadipour and A. Bahrami, *J. Mol. Model.*, 2019, **25**, 1–6.
28 O. Rahaman, B. Mortazavi, A. Dianat, G. Cuniberti and T. Rabczuk, *Nanotechnology*, 2016, **28**, 055707.
29 R. Baughman, H. Eckhardt and M. Kertesz, *J. Chem. Phys.*, 1987, **87**, 6687–6699.
30 O. Rahaman, B. Mortazavi, A. Dianat, G. Cuniberti and T. Rabczuk, *FlatChem*, 2017, **1**, 65–73.
31 A. Bafekry, M. Faraji, M. M. Fadlallah, H. R. Jappor, S. Karbasizadeh, M. Ghergherehchi and D. Gogova, *J. Phys.: Condens. Matter*, 2021, **34**, 015001.
32 D. Ferguson, D. J. Searles and M. Hankel, *ACS Appl. Mater. Interfaces*, 2017, **9**, 20577–20584.
33 C. Ashraf and A. C. Van Duin, *J. Phys. Chem. A*, 2017, **121**, 1051–1068.
34 S. Plimpton, *J. Comput. Phys.*, 1995, **117**, 1–19.
35 T. P. Senftle, S. Hong, M. M. Islam, S. B. Kylasa, Y. Zheng, Y. K. Shin, C. Junkermeier, R. Engel-Herbert, M. J. Janik, H. M. Aktulga, *et al.*, *npj Comput. Mater.*, 2016, **2**, 1–14.
36 B. D. Jensen, K. E. Wise and G. M. Odegard, *J. Phys. Chem. A*, 2015, **119**, 9710–9721.
37 B. D. Jensen, K. E. Wise and G. M. Odegard, *J. Comput. Chem.*, 2015, **36**, 1587–1596.
38 J. Rimsza, J. Yeon, A. Van Duin and J. Du, *J. Phys. Chem. C*, 2016, **120**, 24803–24816.
39 N. Dasgupta, Y. K. Shin, M. V. Fedkin and A. C. van Duin, *Comput. Mater. Sci.*, 2020, **172**, 109349.
40 Y. Luo, C. Ren, Y. Xu, J. Yu, S. Wang and M. Sun, *Sci. Rep.*, 2021, **11**, 1–6.
41 W. G. Hoover, *Phys. Rev. A*, 1985, **31**, 1695.
42 M. L. P. Júnior and L. A. R. Júnior, *FlatChem*, 2020, **24**, 100196.
43 R. v. Mises, *Math.-phys. Klasse*, 1913, **4**, 582–592.
44 LAMMPS Documentation, https://docs.lammps.org/Manual.html, 2021, [online; accessed 17-September-2021].
45 J.-L. Tsai and M.-J. Sie, *J. Nanosci. Nanotechnol.*, 2015, **15**, 3764–3772.
46 W. Humphrey, A. Dalke and K. Schulten, *J. Mol. Graphics*, 1996, **14**, 33–38.
47 T. Han, T. Jiang, X. Wang, P. Li, L. Qiao and X. Zhang, *Mater. Res. Express*, 2019, **6**, 095619.
48 B. Witkowska and I. Frydrych, *Soft Computing in Textile Engineering*, Elsevier, 2011, pp. 424–489.
49 F. Memarian, A. Fereidoon and M. D. Ganji, *Superlattices Microstruct.*, 2015, **85**, 348–356.
50 B. Mortazavi and S. Ahzi, *Carbon*, 2013, **63**, 460–470.
51 Y. Zhang and C. Pan, *Diamond Relat. Mater.*, 2012, **24**, 1–5.
52 C. Lee, X. Wei, J. W. Kysar and J. Hone, *science*, 2008, **321**, 385–388.
53 A. Falin, Q. Cai, E. J. Santos, D. Scullion, D. Qian, R. Zhang, Z. Yang, S. Huang, K. Watanabe, T. Taniguchi, *et al.*, *Nat. Commun.*, 2017, **8**, 1–9.
54 A. Castellanos-Gomez, M. Poot, G. A. Steele, H. S. Van Der Zant, N. Agraït and G. Rubio-Bollinger, *Adv. Mater.*, 2012, **24**, 772–775.
55 L. C. Felix, R. M. Tromer, P. A. Autreto, L. A. Ribeiro Junior and D. S. Galvao, *J. Phys. Chem. C*, 2020, **124**, 14855–14860.
56 J. Los, K. Zakharchenko, M. Katsnelson and A. Fasolino, *Phys. Rev. B: Condens. Matter Mater. Phys.*, 2015, **91**, 045415.
57 E. Ganz, A. B. Ganz, L.-M. Yang and M. Dornfeld, *Phys. Chem. Chem. Phys.*, 2017, **19**, 3756–3762.
58 Y. D. Fomin and V. Brazhkin, *Carbon*, 2020, **157**, 767–778.